nature electronics

Article

https://doi.org/10.1038/s41928-026-01655-8

A wirelessly powered, light-controlled, bioresorbable stimulation system with programmable polyphasic waveforms

Received: 29 March 2025

Accepted: 14 May 2026

Published online: 16 June 2026

Check for updates

Jong Uk Kim[1,2,36], Seung Gi Seo[1,3,36], Hongkai Wang[4,36], Eric Rytkin[5,36], Jiarui Gong[6,7], Jie Zhou[6,8], Junhwan Choi[1,9,10], Jiwon Kim[1,2], Sun Young Park[1,11], Anna Pfenniger[12], Rishi K. Arora[13], Aleksei Mikhailov[13], Jinheon Jeong[1,14,15], Seungyeob Kim[16], Yamin Zhang[1,17], Ravi F. Nuxoll[1,18,19], Hak-Young Ahn[1], Geumbee Lee[1,20], Shupeng Li[21], Dae-Hyeon Song[1,22], Sangwon Cha[1,23], Young Jin Jo[1], Sang Min Won[24], Tae-il Kim[2], Yei Hwan Jung[11], Sumanas W. Jordan[25,26], Yonggang Huang[1,18,21,27], Jae-Young Yoo[1,28] ✉, Igor R. Efimov[1,5,29] ✉, Colin K. Franz[1,4,30,31,32,33] ✉, Zhenqiang Ma[6] ✉, Sung Hun Jin[34] ✉ & John A. Rogers[1,5,18,27,35] ✉

Wireless bioresorbable systems for electrical stimulation can deliver electrotherapy over clinically relevant timeframes, and then subsequently dissolve away in a harmless fashion. Such systems have previously been used in neuroregeneration and cardiac pacing, delivering monophasic pulses to a targeted site. Here we report a wirelessly powered system with programmable control of the stimulation waveforms using tissue-penetrating near-infrared light. The approach relies on a bioresorbable silicon phototransistor that is designed to optically modulate current flows at critical nodes in electrical circuits. We show that the approach can offer precise control over stimulation pulses—allowing monophasic, biphasic and polyphasic waveforms to be delivered to single or multiple sites—and all with power wirelessly delivered to a single receiver unit. Using small and large animal models, we further show that the technology enables single- and dual-chamber cardiac pacing, as well as phrenic neuromuscular stimulation for inducing and blocking diaphragmatic excursion.

Physically transient materials, components and integrated systems—which can be reabsorbed harmlessly in the body—can provide diverse biomedical technologies that act as temporary implants[1–5]. They have previously been used to create sensors for monitoring intracranial pressure[6], spectrometers for tracking tissue homeostasis[7], systems for programmed drug delivery[8,9], and electrical stimulators for neuroregeneration[10,11] and cardiac pacing[12–14]. Wireless power transfer techniques are important for many of these systems. One such technique uses inductive magnetic coupling between an external transmitting coil powered by a radiofrequency (RF) supply and a receiving coil integrated within the bioresorbable electronic platform. This approach has, in particular, been used to create electrical stimulators that are designed to produce monophasic pulses for nerve regeneration or cardiac electrotherapy. In this method, the power waveform applied to the transmitting coil defines the duration and frequency of the stimulation pulses through control of the power received by

A full list of affiliations appears at the end of the paper. ✉e-mail: jy.yoo@skku.edu; igor.efimov@northwestern.edu; cfranz@sralab.org; mazq@engr.wisc.edu; jinsh@khu.ac.kr; jrogers@northwestern.edu

the receiving coil[11,12,15]. Closed-loop operation can be achieved with skin-interfaced devices that can sense and transmit RF power, enabling operation even at deep tissue locations owing to low RF absorption in the relevant frequency ranges[15].

This scheme can generate monophasic pulses, but it is difficult to generate the complex stimulation waveforms that are required for many clinical applications[16–18]. Charge-balanced biphasic and polyphasic waveforms are, for instance, recognized for their operational safety[19,20] and energy efficiency, and are of extensive use, for example, in cardiac stimulation[21–23]. The development of programmed multisite stimulation with defined latency with a single device is a further issue that needs to be addressed. Using multiple receiving coils that resonate at different frequencies could provide a solution, but this approach is constrained by device size, structural complexity and limited scalability.

In this Article, we report a bioresorbable silicon (Si) electronic transistor that can remotely control waveforms produced by a stimulator powered by wireless inductive transfer through a single receiving coil. In particular, we use a bipolar junction transistor that functions as a bioresorbable phototransistor (b-PT) and can control the current flow and/or polarity within a targeted node of a circuit in real time. The device can be activated by controlled near-infrared (NIR) illumination within the first transparency window for tissue, allowing operation at deep tissue locations. Compared with an implantable pulse generator or a commercial external generator (Supplementary Table 1), this approach can achieve various stimulation conditions, including monophasic pulses at single or multiple sites, as well as biphasic and polyphasic waveforms across diverse electrical stimulation scenarios (Supplementary Table 2). We use the approach to fabricate a cardiac pacemaker and place it in a canine model for single-, dual-chamber and biventricular stimulation through programmable monophasic and biphasic waveforms. In this example, a wireless, skin-interfaced device with a pair of light-emitting diodes (LEDs), sensors and control modules illustrates a potential route toward closed-loop operation. We also demonstrate monophasic and polyphasic stimulation of the phrenic neuromuscular system (PNMS) in rat models, to validate the efficacy in diaphragm pacing and phrenic nerve (PN) conduction blocking tailored to various cases of diaphragm dysfunction (DD)[24–26].

Wireless, light-controlled, bioresorbable electrical stimulator for polyphasic pulse stimulation

Figure 1a shows the engineering design for the stimulator, which involves b-PTs, a pair of electrodes and a receiving coil. The skin-interfaced device integrates a NIR LED and a transmitting coil, to allow optical switching and wireless power transfer to deep tissue locations. The b-PTs incorporate vertical bipolar junctions (Si PNP-phototransistor; that is, emitter (E; p^+-doped (>10^{19} boron ions cm^{-3})), base (B; n-doped (<10^{17} phosphorus ions cm^{-3})) and collector (C; p-doped (~10^{15} boron ions cm^{-3})); Fig. 1b, left) in which holes (h^+) pass from E to C by diffusion and drift upon exposure to light (Fig. 1b, right), thereby generating photocurrent (I_{ph}). Design optimization follows from modelling of the impurity doping and activation processes (that is, ion implantation, dopant activation and solid diffusion doping; for details, see the Methods, Supplementary Figs. 1 and 2, Supplementary Note 1 and Supplementary Table 3) and from measuring the device operation, to enable high performance in ultrathin b-PTs with small light-responsive regions (width, length and thickness of Si are 500 µm, 500 µm and 5 µm, respectively). Passivation consists of sputter-deposited layers of SiO_2 (200 nm thick); the E and C terminals consist of sputter-deposited films of tungsten (W, 200 nm thick).

Figure 1c displays a sequence of images of the complete dissolution of a b-PT (width 1.4 mm, length 2.6 mm) mounted on a bioresorbable substrate (that is, polyanhydride (PA), 100-µm thick) during accelerated testing that involves immersion in phosphate-buffered saline (PBS, pH 7.4) at 95 °C (Fig. 1c, top right). The chemistries of dissolution associated with these materials appear elsewhere[1,27]. These b-PTs provide versatile capabilities in light-controlled operation of bioresorbable electronic systems (Fig. 1d), each of which uses wireless RF power transfer from an external transmitting coil to an implanted receiving coil, converted to direct current (d.c.) output by passage through a rectifying diode and smoothing capacitor. (i) A device of this type with a single b-PT can yield monophasic stimulation waveforms defined by corresponding temporal patterns of light exposure. As examples, rectangular, triangular and sinusoidal pulses can be generated in a programmable manner through control of current applied to an LED that illuminates the b-PT (electrode module #1, top). (ii) A device with multiple branches, consisting of a pair of b-PTs (two devices) for each stimulation electrode pair can produce multisite monophasic stimulation using power from a single receiving coil, with or without timing differences through the control of multiple LEDs (electrode module #2, bottom left). (iii) A device with an electrode pair connected by a pair of cross-coupled branches (a total of four b-PTs) can generate polyphasic pulses such as monophasic, biphasic and even alternating current (a.c.) outputs with frequencies suitable for broad applications in electrical stimulation (electrode module #3, bottom right). These options support a wide range of shaped stimulation pulses and multisite operation, all with a compact form factor with a single receiving coil. Of particular interest are polyphasic stimulation pulses (for example, biphasic stimulation or a.c. stimulation) designed to minimize damage to targeted tissues and/or surrounding organs, due to their charge-balanced operation.

Fabrication and characterization of b-PTs

Fabrication of b-PTs relies on conventional semiconductor processing methods and the techniques of transfer printing reported previously, as summarized in Fig. 2a and Supplementary Fig. 3: (i) a p-type silicon-on-insulator (SOI) wafer (1–10 Ω cm) with a 5-µm-thick top Si layer serves as the starting substrate; (ii) b-PTs are fabricated through n-doping (phosphorus), p^+-doping (boron) and the deposition and patterning of SiO_2 and W; (iii) removal of the buried oxide (BOX) layer of the SOI wafer by immersion in 49% HF solution creates freestanding structures prepared for transfer printing; and (iv) the transfer-printing process delivers the b-PTs onto the bioresorbable substrate. A buffer region (relatively low boron doping concentration; ~10^{15} boron ions cm^{-3}) with microscale circular patterns shields the p^+ regions from direct contact with the HF solution during BOX etching, which may lead to damage to heavily boron-doped Si regions via electrochemical reaction and mechanisms (Supplementary Fig. 4). Additional details are provided in Supplementary Note 2 and Supplementary Fig. 5. Figure 2b shows plots of the concentrations of dopants (phosphorus (P, red) and boron (B, black)) as a function of depth from the surface of emitter, as estimated by secondary ion mass spectrometry (SIMS). Depth profiling indicates vertical bipolar junctions among E, B and C at depths of approximately 400 nm and 1,200 nm, respectively, consistent with Silvaco TCAD simulation. Figure 2c shows b-PTs on various bioresorbable substrates (for example, PA, poly(lactic-co-glycolic) acid (PLGA), polylactic acid (PLA) and dynamic covalent polyurethane (DCPU)). The current–voltage (I–V) characteristics of representative b-PTs in Fig. 2d indicate negligible differences before and after transfer to PA. A parallel connection of b-PTs proportionally increases the output photocurrent with the number of b-PTs (Supplementary Fig. 6). Figure 2e describes I–V characteristics of a three-parallel (3P) b-PT for various intensities of illumination from light of an 850-nm-wavelength LED ranging from dark to 50 mW cm^{-2}. The resistance of the 3P b-PT decreases from tens of megaohms (MΩ) in the dark and saturates at a few kiloohms (kΩ) under illumination (Fig. 2f). Measurements using LEDs with various wavelengths at a fixed intensity of 10 mW cm^{-2} (Supplementary Fig. 7a,b) and a voltage between the emitter and collector (V_{EC}) of 2.0 V indicate that the relative response (%), normalized to maximum current

https://doi.org/10.1038/s41928-026-01655-8

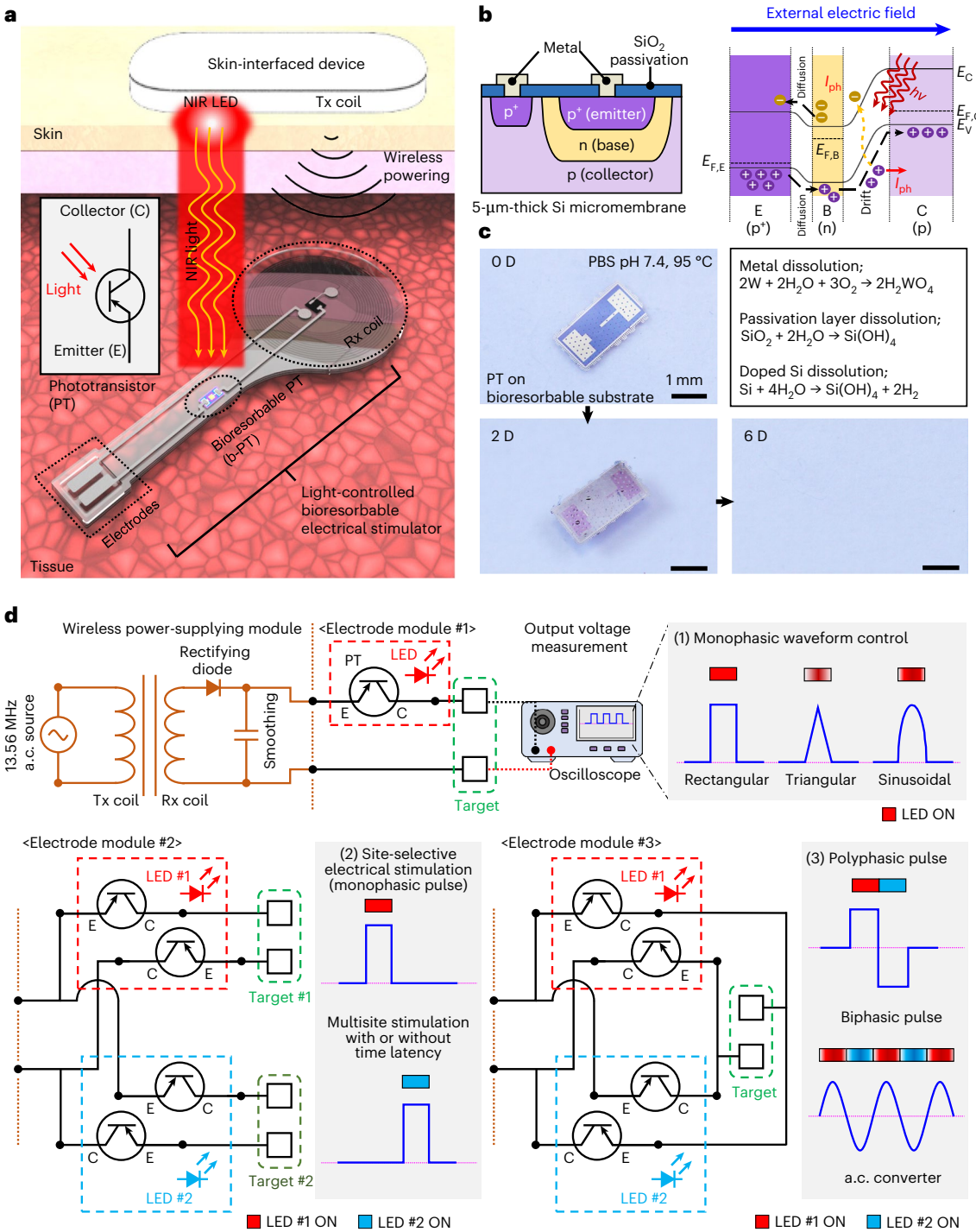

Fig. 1 | Wireless, light-controlled, bioresorbable devices for electrical stimulation with programmable polyphasic waveforms. a, Schematic illustration of the operating principle of the device, which incorporates an ultrathin (5 μm) b-PT with RF-receiving coil (Rx) for external control by a skin-interfaced unit that incorporates an NIR LED and RF-transmitting coil (Tx) for wireless power transfer. **b**, Cross-sectional schematic illustration (left) and the energy-band diagram (right) of the b-PT. This silicon device includes a metal pad (tungsten), SiO_2 passivation layer, E (p^+ (boron)-doped), B (n (phosphorus)-doped) and (p (boron)-doped) regions. **c**, Dissolution of a printed b-PT on a bioresorbable substrate (that is, PA) and associated chemical reactions with surrounding PBS (pH 7.4) at 95 °C. **d**, Circuit diagrams of stimulators with three different electrode modules for (i) monophasic pulse control (top right), (ii) multisite electrical stimulation (bottom left) and (iii) polyphasic waveform generation (bottom right). E_C, conduction band energy; E_V, valance band energy, $E_{F,E}$, Fermi level of emitter; $E_{F,B}$, Fermi level of base; $E_{F,C}$, Fermi level of collector.

output, is the highest in the 600-nm-wavelength regions (Fig. 2g and Supplementary Fig. 7c,d). These responses are consistent with simulation results (Supplementary Fig. 8). Wavelengths in the first NIR biological transparency window (typically 750–900 nm)[28–30] are particularly effective for deep tissue penetration because of their relatively low absorption and scattering compared with visible light[31]. Supplementary Fig. 9 indicates that light attenuation through a biological tissue (for example, chicken breast) is relatively lower at 850 nm than at 623 nm. Accordingly, 850-nm NIR illumination was used for subsequent device characterizations to enable reliable optical

https://doi.org/10.1038/s41928-026-01655-8

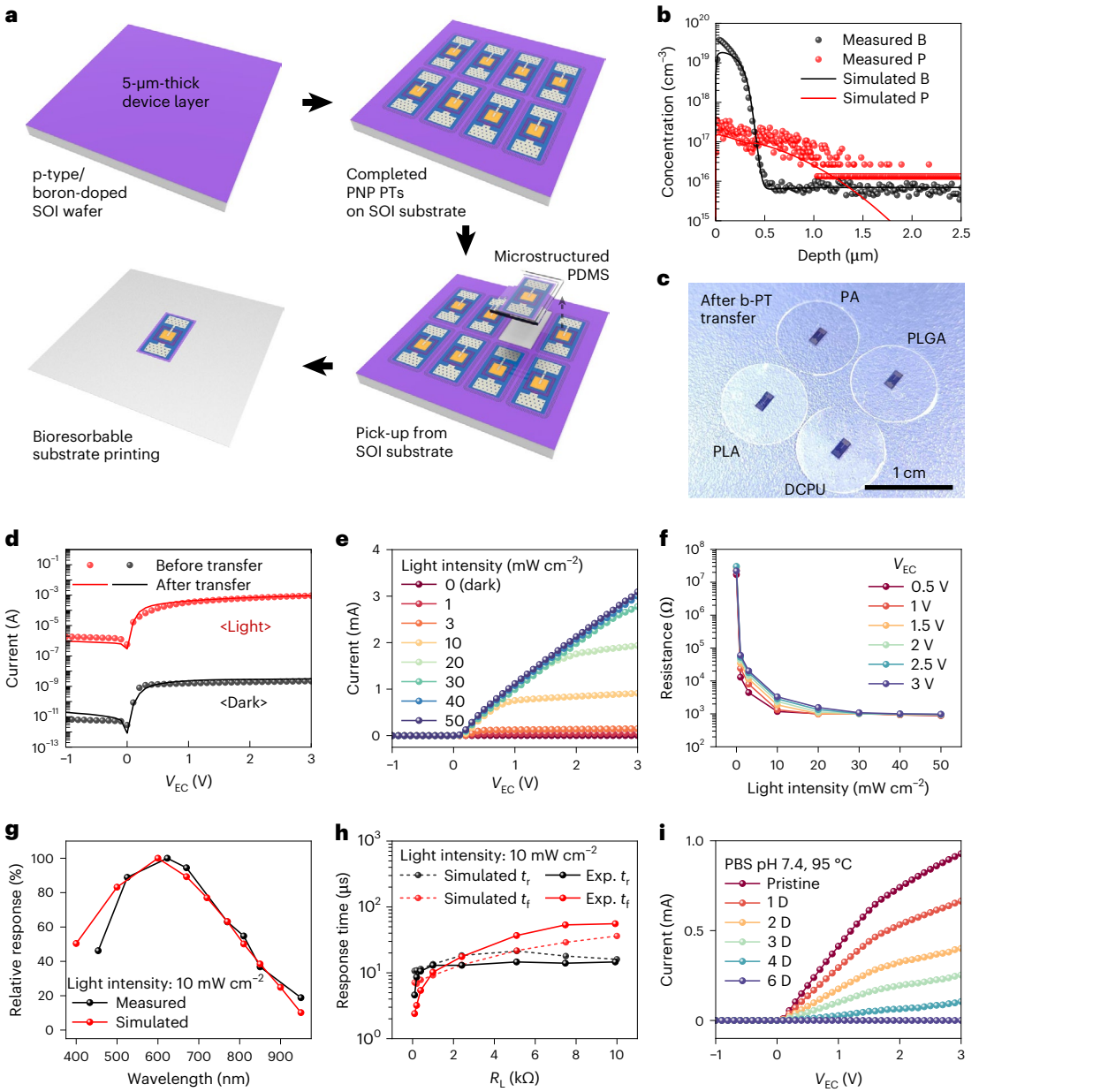

Fig. 2 | Fabrication processes and performance characteristics of b-PTs. **a**, Schematic illustration of the steps for forming a single b-PT on a bioresorbable substrate. **b**, Doping phosphorus (red) and boron (black) concentration profiles, estimated by SIMS and simulation as a function of the depth of the silicon phototransistor. **c**, Photographs of transferred b-PTs on various bioresorbable substrates. **d**, Photocurrent output of a b-PT before and after transfer printing under dark (black) and light (red) conditions. **e**,**f**, Photocurrent output and estimated resistances of a collection of three b-PTs connected in parallel (3P b-PT) as a function of light intensity between 0 mW cm^{-2} to 50 mW cm^{-2}. **g**, Wavelength dependence of a b-PT under a light intensity of 10 mW cm^{-2} with wavelengths from 400 nm to 950 nm. Black and red lines are experimental (Exp.) and simulation data, respectively. **h**, Dependence of t_r (black) and t_f (red) times as a function of R_L. The dashed and solid lines represent the simulated and experimental results, respectively. **i**, Current–voltage characteristics of a b-PT for various times of immersion in PBS (pH 7.4) measured in days (D) at a temperature of 95 °C. PDMS, polydimethylsiloxane.

control of implanted devices in in vivo settings. As the pulse width and phase duration can also vary across the clinical applications (for example, biphasic pulse widths in the tens of microseconds of cochlear implant[32]), the response times, including both the rising (t_r) and falling (t_f) times, are important in generating precise polyphasic pulse waveforms. Supplementary Fig. 10a illustrates a benchtop set-up that mimics an optocoupler circuit for testing these response times. An oscilloscope records the voltage (V_L) across a load (R_L) that simulates the resistance of targeted tissue (0.1–10 kΩ) between the stimulation electrodes during cycles of fast switching of the LED (see Supplementary Note 3 and Supplementary Fig. 10b for a detailed description). Figure 2h shows the dependence of these two times on R_L. The value of t_r gradually increases and saturates at 15 μs with increasing R_L. The value of t_f shows a similar trend, but slightly less than and larger than t_r for low and high values of R_L, respectively, consistent with simulated trend of t_r and t_f (see dashed lines in Fig. 2h and Supplementary Fig. 11). The results indicate that the b-PT-integrated electrical stimulator can produce polyphasic pulses with time resolutions in the tens of microseconds, provided that the stimulation electrodes exhibit relatively low impedance across the target tissues. As for the temperature-dependent b-PT performance, the photocurrent shows minimal variation between 30 °C and 45 °C (approximately 60 μA increase (~5%); Supplementary Fig. 12). Although modest shifts are observed at more than 60 °C, the current remains within expected output (~1 mA photocurrent) even at 90 °C. Figure 2i

shows that the photocurrent of a single b-PT gradually decreases during accelerated testing in PBS (pH 7.4) at 95 °C. Calculated timescales for complete bioresorption are ~0.6–1.25 years and ~2.7 years in artificial cerebrospinal fluid and PBS at 37 °C, respectively[6,27,33].

Light-controlled polyphasic waveform generation for electrical stimulation

Figure 3a shows an exploded-view illustration and photograph of a monolithically integrated, bioresorbable, wireless electrical stimulator. The surface of the partially ultraviolet (UV)-cured PA[34], serving as an encapsulant, contains abundant acrylic functional groups (C=C), thus enabling the formation of a double-layered receiving coil by folding the top and bottom layers across the hinge (Fig. 3a, bottom left inset; details in the Methods and Supplementary Fig. 13). Supplementary Fig. 14 shows the characteristics of the receiving coils including the finite element analysis-simulated impedance, quality (Q) factor and measured scattering parameter (S11). The device consists of a receiving coil of Mo (25-μm thick), a Si PIN diode (5-μm thick), a Si capacitor (5-μm thick), b-PTs (5-μm thick), interconnects of Mo (15-μm thick) and W/Candelilla wax conductive paste (approximately 12:1 weight ratio). The components support wireless power harvesting, a.c.-to-d.c. conversion, smoothing of the rectified voltage and optical switching. All functional materials (Mo, Si, SiO_2, Candelilla wax and W) and the encapsulant/substrate (PA) are bioresorbable. The device completely disappears in PBS solution (pH 7.4), with stable operating times defined largely by the compositions and thicknesses of the PA encapsulants[34,35].

Testing of these devices confirms the operational capability mentioned in the context of Fig. 1d, where optical activation uses two NIR LEDs (Fig. 3b, 850-nm-wavelength LEDs #1 and #2) mounted onto a flexible printed circuit board (fPCB). The red and blue boxes indicate times when LED #1 and LED #2 are on, respectively. For a 3.3 V driving voltage to the LED with 1 ms pulse width over 1 min, the temperature increases for frequencies ranging from 3 Hz (0.3% duty cycle) to 50 Hz (5% duty cycle) are negligible (Supplementary Fig. 15). The 20-mm spacing between the b-PT pairs shown in Fig. 3a allows spatially selective illumination. When the lateral spacing between two b-PTs is 20 mm, positioning the LED at heights (h) of 6 mm and 18 mm above the b-PT reduces the photocurrent by up to 0.1% and 2.8%, respectively, relative to the b-PT located directly beneath the LED (Supplementary Fig. 16). These results indicate that, at shallow tissue depths (<~18 mm), tissue-induced light scattering does not appreciably compromise the independent operation of each b-PT pair. Nevertheless, for deep-tissue operation, scattering can induce non-negligible crosstalk between neighbouring b-PT nodes, indicating that additional strategies are required. As an additional option, bioresorbable optical filters can be placed over the b-PTs to allow wavelength-selective illumination, to further reduce the possibility for crosstalk (Supplementary Fig. 17).

RF a.c. voltage (Fig. 3c; peak-to-peak voltage (V_{pp}) of 5 V at 13.56 MHz, black line) applied to the transmitting coil wirelessly delivers power to the receiving coil, thereby creating a d.c. monophasic output defined by the diode rectifier, but with some residual RF fluctuation in the voltage (Fig. 3c, V_{pp} = 1 at 13.56 MHz, red line). The Si capacitor (200 pF; Supplementary Fig. 18a,b) largely eliminates these fluctuations, from an amplitude of 1 V to 0.25 V, while the mean voltage increases from 4.6 V to 5.4 V (Supplementary Fig. 18c) as an approximate d.c. output (Fig. 3c, V_{pp} = 0.25 at 13.56 MHz, blue line). The monophasic output can be manipulated by adjusting the output of the single NIR LED. As shown in Supplementary Fig. 19a, various waveforms are possible, such as rectangular (pulse width 5 ms and 1 ms, respectively), triangular (pulse width 5 ms, increase 50% and decrease 50%) and sinusoidal pulses (pulse width 5 ms) by applying temporally modulated light intensity from the LED. Supplementary Fig. 19b illustrates a strategy for light-controlled multisite stimulation with such types of monophasic pulse. Time-shifted or synchronized output from a pair of NIR LEDs yields monophasic pulses for dual-point stimulation with adjustable parameters that include pulse period (x), pulse width (y_1, y_3), relative timing of each pulse (y_2) and pulse amplitude (z_1, z_2). Modulating LEDs #1 and #2 (Fig. 3d, where x is 300 ms, and y_1 and y_3 are 3 ms, marked with red and blue boxes, respectively) produces monophasic pulses for multisite stimulation, for specific cases such as similar output voltages (both z_1 and z_2 are 5 V) with a y_2 of 77 ms. Furthermore, Fig. 3e,f indicates the ability to deliver monophasic pulses without time–latency and with different amplitudes through corresponding control of the LEDs, such as $z_2 = 0.5 \times z_1$. This level of adjustability over stimulation parameters at multiple target sites creates potential applications that range from post-stroke hemiplegia treatment[36,37], to obesity control[38], cardiac pacing[39] and perception studies for patients with hand loss[40].

Supplementary Fig. 19c illustrates methods for generation of polyphasic waveforms. The voltage across one electrode pair, connected by two cross-coupled pairs of b-PTs, can rapidly vary between anodic and cathodic pulses by activating LEDs #1 and #2, respectively. Figure 3g shows biphasic pulses generated in this manner (V_{pp} = 10 V; both y_1 and y_3 are 3 ms) with and without interphase time delay (y_2 = 3 ms). In addition, by varying the voltage supplied to the LEDs, such as in a sinusoidal fashion, the anodic and cathodic pulses from the two pairs of b-PTs can be transformed into a.c. output. Based on the measured response times (that is, t_r and t_f) of these b-PTs (Fig. 2h), this strategy can produce a.c. outputs with frequencies into the kilohertz range, suitable for blocking nerve conduction. Figure 3h demonstrates a.c. output with a V_{pp} = 10 V at frequencies of 10 kHz, 25 kHz and 50 kHz. Supplementary Fig. 20 presents precise controls of output V_{pp} ranging from 1 to 10 V at a fixed frequency of 10 kHz. Estimated temperature increases of the LED during 50-kHz waveform generation for 1 h are approximately 2 °C (Supplementary Fig. 15).

In vivo cardiac pacing demonstration with monophasic and biphasic pulses

In vivo studies on a canine model during open-chest surgery involve an implanted bioresorbable electrical stimulator designed for single- and dual-location cardiac pacing with polyphasic pulses (for example, monophasic and biphasic pulses). Wired recordings of electrocardiogram (ECG) data capture the electrical activity of the heart throughout the period of the experiments (Fig. 4a). RF power at 13.56 MHz applied to the transmitting coil serves as the basis for wireless power transfer to the receiving coil of the pacemaker. Stimulation electrodes affixed at appropriate pacing positions using either suturing or bioadhesives enable light-controlled pacing. Based on R_L measurements shown in Supplementary Fig. 21, the resistances of the targeted epicardial tissue in both small and large animal models are in the range of 1–2 kΩ at a V_{in} of 0.6 V or higher. Supplementary Fig. 22 shows subcutaneous implantation of a wireless stimulator at a depth of approximately 10 mm with placement of a wearable device. This device incorporates two NIR LEDs (850-nm-wavelength LEDs #1 and #2) and Bluetooth electronics for wireless operation via a smartphone interface, allowing the illumination times and operating frequencies of each LED to be set (see bottom insets in Fig. 4a and Supplementary Fig. 23a,c). Supplementary Fig. 24 shows variations in photocurrent output of the b-PT at an applied V_{EC} of 0.8 V with increasing chicken tissue depth using the wearable device, which rests on the shaved skin of the animal above the location of the implanted pacemaker. Figure 4b,c shows bioresorbable pacemakers in monophasic dual-point and polyphasic single-point modes (see detailed design and wireless power transfer characteristics in Supplementary Note 4 and Supplementary Figs. 25 and 26).

Programmable control enabled by the b-PTs enables latency-adjustable cardiac pacing using monophasic pulses in both simultaneous and sequential settings. Examples include simultaneous biventricular (BiV; left ventricle (LV) + right ventricle (RV)) and sequential atrioventricular (A&V; left atrium (LA) + RV) pacing (Fig. 4d,e and Supplementary Fig. 19b). Figure 4d–f and Supplementary Fig. 27 present

https://doi.org/10.1038/s41928-026-01655-8

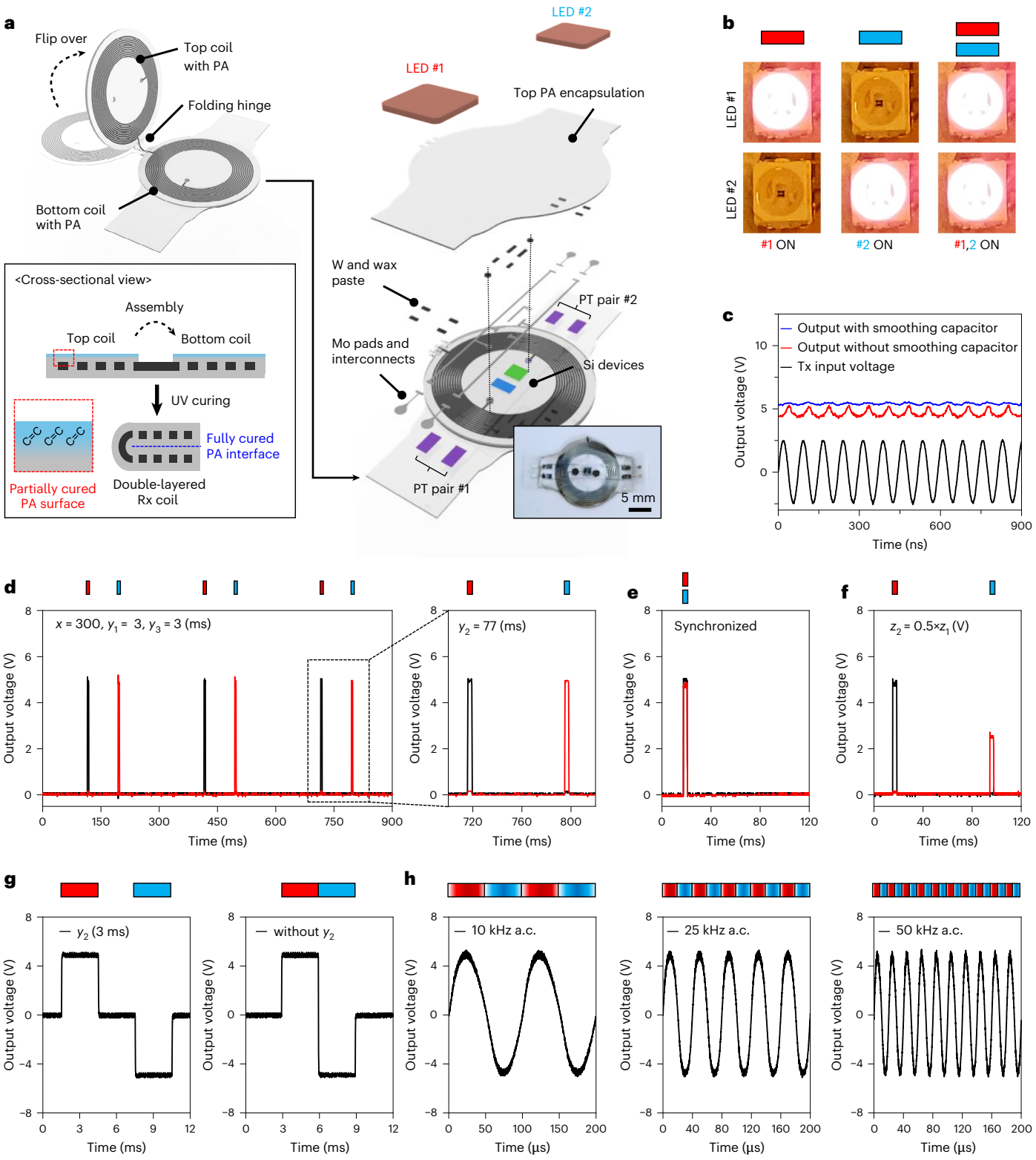

Fig. 3 | Experimental demonstrations of light-controlled waveform generation for electrical stimulation. a, Schematic illustration of a device. Inset: photograph of the device. **b**, Photographs of the LEDs to induce optical switching of the b-PT. The red and blue boxes indicate activation of LED #1 and LED #2, respectively. **c**, Representative output waveforms with (blue) or without (red) a metal oxide semiconductor (MOS) capacitor (200 pF) to smooth the rectified voltage wirelessly generated by an a.c. voltage (black; V_{pp} = 5 V; 13.56 MHz) applied to the transmitting coil. **d**–**f**, Light-controlled monophasic pulse generation for multisite, time-delayed (y_2 = 77 ms, **d**) or synchronized (**e**) electrical stimulation and its adjustable pulse amplitude ($z_2 = 0.5 \times z_1$; **f**). **g**, Light-controlled biphasic pulse generation with (left) and without (right) interphase delay (y_2) for electrical stimulation. **h**, Light-controlled a.c. output at different frequencies (10 kHz (left), 25 kHz (centre) and 50 kHz (right)).

ECG recordings of the intrinsic sinus rhythm (~162 beats per minute, bpm) and of different pacing modes, respectively. Single LED operation with a pulse period (x) of 300 ms enables both RV-monophasic (M) (RV-M; 200 bpm, Fig. 4d, left) and LV-M pacing (LV-M; 200 bpm, Fig. 4d, centre) modes by activating LED #1 (pulse width (y_1) of 1 ms) and LED #2 (pulse width (y_3) of 1 ms), respectively. The simultaneous operation of dual LEDs with x = 300 ms and y_1, y_3 = 1 ms provides synchronized BiV-M pacing (Fig. 4d, right), supporting cardiac resynchronization therapy in patients with electrical conduction delays between left and right bundle branches. ECG results for BiV-M pacing present a narrowed QRS duration (QRSd 82 ± 6 ms) due to synchronized ventricular depolarization, compared with RV-M (QRSd 133 ± 9 ms) and LV-M pacing (QRSd 112 ± 5 ms; Supplementary Fig. 28). In another example, simultaneous stimulation of both the atrium and ventricle, with a latency of tens of milliseconds between atrial and subsequent ventricular stimulation, can mimic the harmonious pumping action of the heart. This type of sequential pacing mode from LA to RV with dual LEDs with x = 380 ms, y_1, y_3 = 1 ms and a time latency (y_2) of 80 ms is shown in Fig. 4e. A widened QRS morphology after A&V pacing (158 bpm; Fig. 4e, right) is consistent with RV-M pacing (Fig. 4d, left). This result indicates that impulses on both the LA and RV from the pacemaker have the appropriate time latency.

Placing one electrode pair, connected by cross-coupled pairs of b-PTs, onto each wall of the LV and RV serves to validate the use of monophasic and biphasic pulses for single-chamber pacing. Appropriate operating parameters for dual LEDs enable monophasic (x = 300 ms, y_1 = 1 ms) and biphasic (x = 300 ms, y_1, y_3 = 1 ms, and y_2 = 0 ms) pulses. Despite different stimulation waveforms, results of ECG recordings indicate that QRS complexes during monophasic and biphasic pacing of the RV (Fig. 4f) and the LV (Supplementary Fig. 27b) are consistent. The estimated threshold values of input V_{pp} for the transmitting coil at 13.56 MHz to achieve monophasic (Fig. 4g, black bar) and biphasic (Fig. 4g, red bar) pacing at the RV and LV are, however, quite different (see details in Supplementary Note 4 and Supplementary Fig. 29). Specifically, monophasic pulses require a V_{pp} of 5.9 V and 6.1 V to achieve RV-M and LV-M pacing mode, respectively. Biphasic pacing requires a V_{pp} of 4.3 V and 2.5 V for these same cases (Supplementary Fig. 30). Consistent with previous clinical studies, biphasic stimulation is more energy-efficient than monophasic[21,41]. Moreover, such biphasic mode increase cardiac conduction velocity[42] and enable faster, more complete reactivation of the sodium current compared with monophasic pacing[21]. The skin irradiance required to achieve pacing output, based on calculations of maximum permissible exposure for skin safety, indicates that the device can reliably operate at depths of up to approximately 57 mm within the body (Supplementary Figs. 31 and 32 and Supplementary Notes 5 and 6). Improving optical sensitivity of the b-PT by introducing topside anti-reflection/backside reflective layers, increasing the number of b-PTs connected in parallel (Supplementary Fig. 24c) or using NPN-type phototransistors, which exhibit generally higher photocurrents than PNP devices, will allow pacing at deeper locations. An additional option is to increase the stimulation pulse width, which lowers the threshold current, as indicated by the strength–duration curve[14].

In vivo electrical stimulation of PNMS for diaphragm muscle modulation

The PNMS across the mid-cervical spinal cord (C3–C5), the PN and the diaphragm muscle (DM) play critical roles in controlling the diaphragm, the large muscle essential to breathing as well as coughing, swallowing and speaking (Fig. 5a). DD resulting from spinal cord injury, PN neuropraxia or post-lung transplantation surgery has severe effects on patients (Fig. 5b, left). In addition, persistent hiccups caused by involuntary spasmodic contractions lasting weeks or months can lead to respiratory distress, also associated with DD (Fig. 5b, right). The blockage of diaphragm movement also alleviates diaphragmatic pain[43,44]. Electrical modulation of PNMS for diaphragm pacing and functional blocking can be useful in each case, realized with monophasic pulses[45,46] and polyphasic kilohertz-frequency a.c. (KHFAC) waveforms[18], respectively. Supplementary Fig. 33 illustrates electrical modulation of PNMS in rat models using a cuff electrode that wraps the PN to deliver monophasic pulses for diaphragm pacing (Supplementary Fig. 33, inset, red line) or KHFAC waveforms for preventing the propagation of action potentials from the phrenic motor nucleus in the spinal cord to block diaphragm activity (Supplementary Fig. 33, inset, blue line). Guided by previous reports on localized nerve stimulation[11] and conduction block[35], we implemented bipolar and tripolar cuff electrode configurations. The Mo electrodes were 15-µm thick and spaced by 450 µm and 150 µm for the bipolar and tripolar configurations, respectively. This layout facilitates implantation in a limited region (~2 mm) after isolating the PN from the nerve bundle (Supplementary Fig. 34). Figure 5c illustrates a wireless, bioresorbable diaphragm pacer with a design described previously (Fig. 5c, inset) for delivery of monophasic stimulation pulses through a bipolar electrode (Fig. 5d) positioned beneath the PN (Fig. 5d, dashed white line) for diaphragm pacing. Based on R_L measurements shown in Supplementary Fig. 21, the resistances of the targeted PN in small animal models are in the range of 6–9 kΩ at a V_{in} of 1 V. The implantation procedures are described in Supplementary Fig. 35 and the Methods. Unlike cardiac pacing, which requires a single pulse per beat, modulation of DM tension demands high-frequency stimulation, typically in the tens of hertz, per breath (Supplementary Fig. 36). Illumination with the LED at a wavelength of 850 nm with suitable frequency, while continuously supplying RF power through the transmitting coil, generates the appropriate monophasic pulse frequency with a pulse width of 1 ms required for complete tetanus. Ultrasound imaging captures variations in diaphragm excursion (Supplementary Fig. 37a). Depending on the illumination frequency, single twitching (10 Hz), twitching summation (20 Hz) and complete tetanus (50 Hz) occur (Fig. 5e). These results demonstrate that the device can programmably modulate muscle contraction, with potential as a temporary diaphragm pacing system for managing respiratory insufficiency. Stable operation is possible for 10 days (Supplementary Fig. 38), exceeding requirements in temporary pacing for instances in post-lung transplantation surgery and extensive aortic repair[47,48]. Details regarding the in vivo biocompatibility of the device are provided in Supplementary Note 7 and Supplementary Figs. 39–42. For long-term clinical scenarios, more biofluid-resistant encapsulation materials, improved mechanical stability at electrical junctions, and greater electrochemical stability during pulse delivery should be considered to extend device lifetime.

A tripolar electrode configuration (see details in the Methods and Supplementary Fig. 37b), also in a rat model, serves to demonstrate the diaphragm blocking effect via PN modulation. The electrodes include (1) a stimulating needle electrode to induce an action potential, thereby propagating from the proximal to distal PN, (2) a blocking tripolar electrode that wraps the nerve at a location distal to the stimulation point to deliver a polyphasic KHFAC waveform, and (3) a recording needle electrode at the costal insertion of the diaphragm to detect compound muscle action potential (CMAP) amplitude and diaphragmatic electromyogram (EMG). Figure 5f shows variations in CMAP amplitude as a function of V_{pp} of a KHFAC waveform at a frequency of 1 kHz, while applying a supramaximal stimulation current of 1 mA (Supplementary Fig. 43). The blocking effect occurs at 1 kHz with a voltage of V_{pp} = 1 V or higher. CMAP results before and after KHFAC are consistent with the reversibility of this conduction block. Next, removing the stimulating electrode reveals voluntary diaphragmatic motor signals generated at the phrenic neuromuscular junction. In addition to diaphragm EMG, ultrasound imaging and abdominal movement data collected by wearable sensors (for example, inertial measurement unit (IMU)[49,50]; Supplementary Fig. 23b,c) provide further validation of on-demand blocking of diaphragm excursion (Supplementary Table 4). Figure 5g displays variations in right side

https://doi.org/10.1038/s41928-026-01655-8

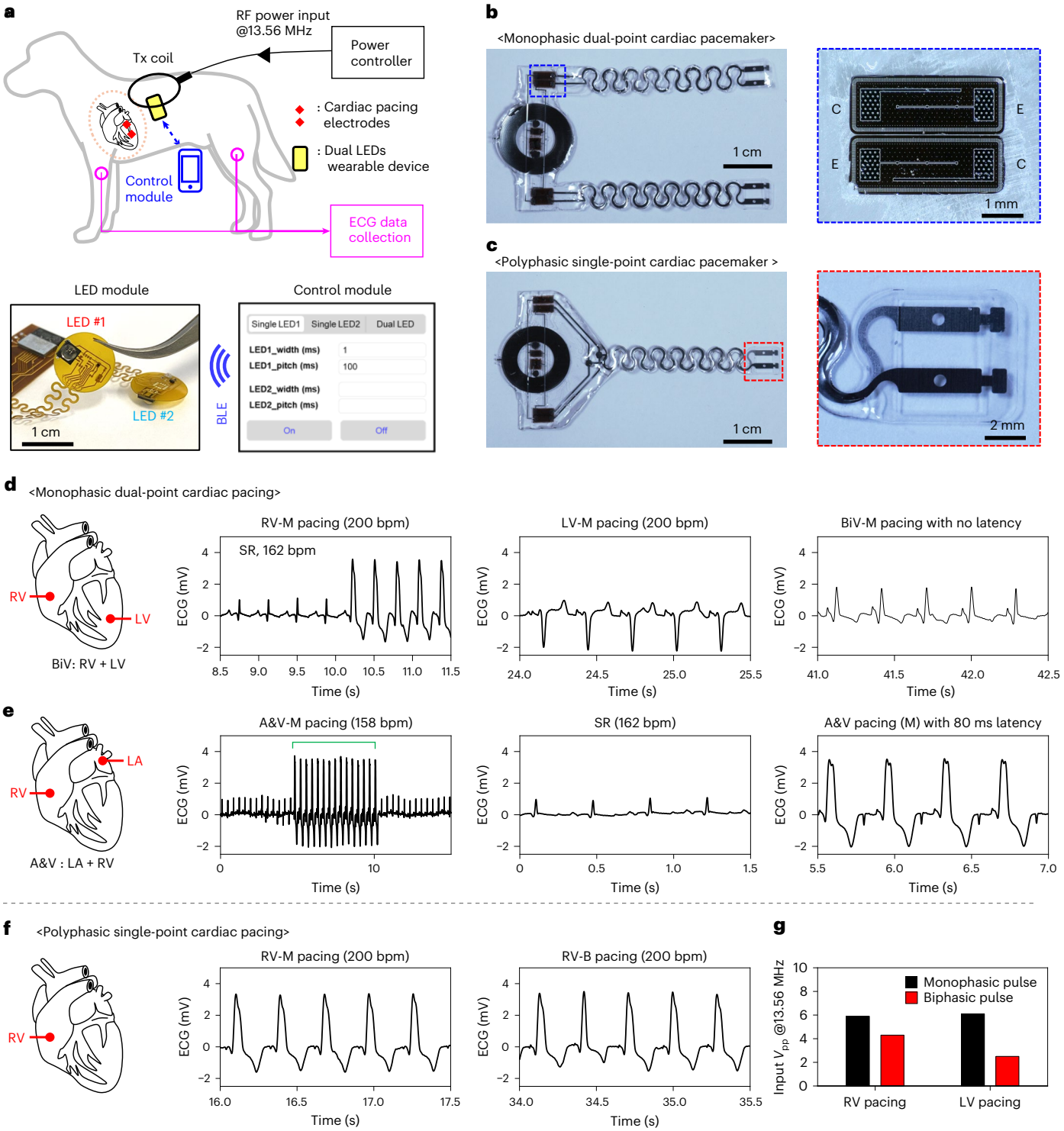

Fig. 4 | In vivo demonstration of single- and dual-point cardiac pacing with polyphasic waveforms in canine models. a, Schematic diagram of the set-up for cardiac pacing and ECG recording. Bottom insets: a wearable device with dual LEDs and a control module with Bluetooth low energy (BLE) communication. **b**,**c**, Photographs of bioresorbable cardiac pacemakers for monophasic dual-point (**b**) and polyphasic single-point (**c**) modes. Top: a pair of b-PTs (C and E regions (**b**). Bottom: stimulation electrodes (**c**)). **d**,**e**, Representative ECG data under sinus rhythm and during latency-adjustable cardiac pacing at dual points with monophasic pulses (that is, BiV with no latency (LV + RV, **d**) and A&V with 80 ms latency (LA + RV, **e**), respectively). **f**, Representative ECG data during single-point cardiac pacing (that is, RV) with polyphasic pulses (monophasic (left) and biphasic (right) pulses, respectively). **g**, Estimated threshold V_{pp} for the transmitting coil to induce monophasic (black) and biphasic (red) pacing at the RV and LV.

diaphragmatic EMG and simultaneous recordings of contralateral (left side) and ipsilateral (right side) abdominal movements via two IMU sensors mounted on opposite sides of an anesthetized rat during KHFAC stimulation (1 kHz, V_{pp} = 1.4 V; yellow box region) of the right PN (Supplementary Fig. 44a). EMG signals per breathing completely disappear (Fig. 5g, top), and ipsilateral acceleration along the *z* axis (Accel. *Z*) recorded by the right IMU #2 approaches zero, indicating successful blocking of voluntary diaphragm excursion (Fig. 5g, bottom).

https://doi.org/10.1038/s41928-026-01655-8

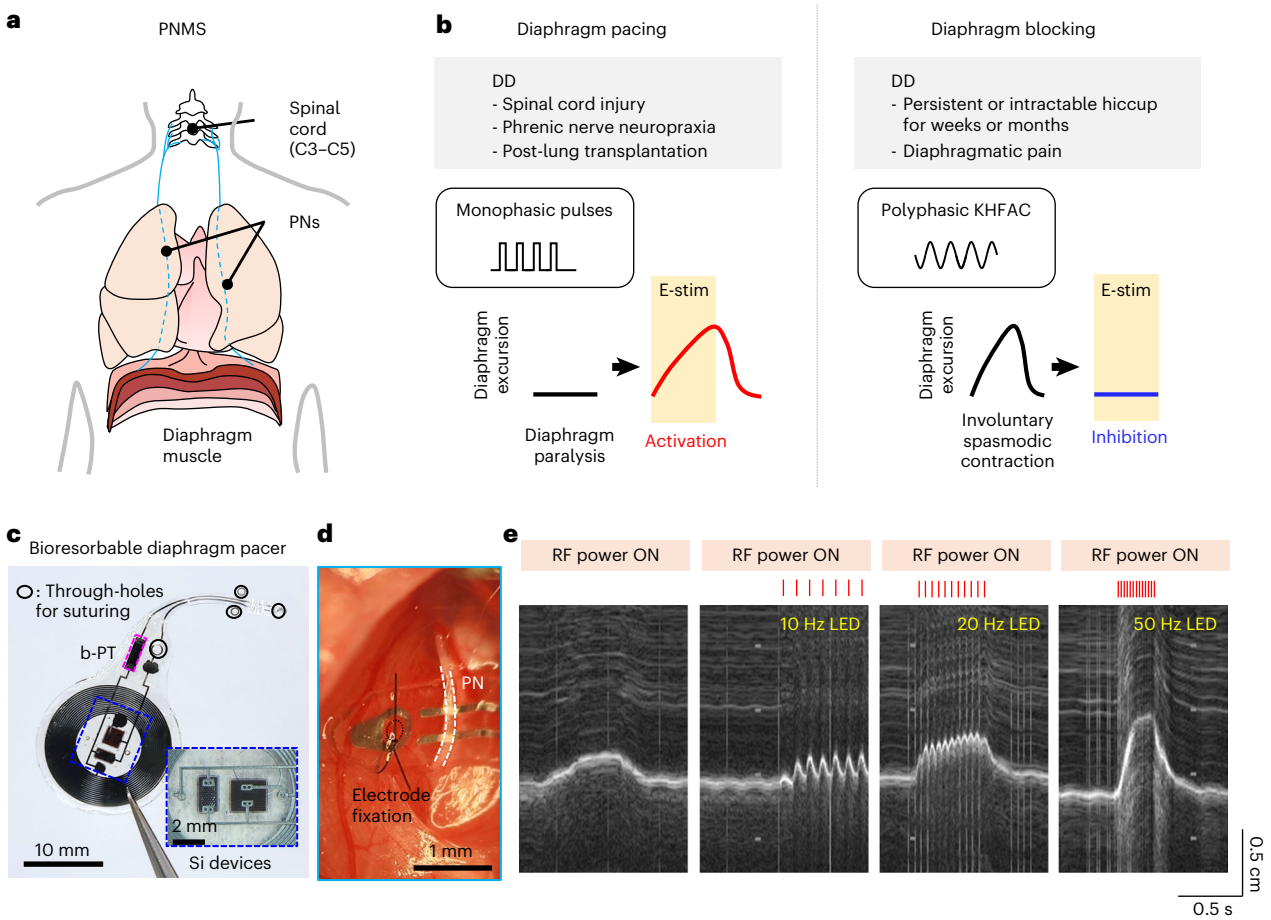

Fig. 5 | Light-controlled electrical stimulation of the PNMS. a, Schematic illustration of the PNMS in a human participant including the mid-cervical spinal cord (C3–C5), the PN and the DM. **b**, Electrical stimulation (E-stim) strategies for diaphragm pacing and PN conduction blocking utilizing monophasic pulses and polyphasic KHFAC, respectively, designed for various cases of DD. **c**, Photographs of a bioresorbable diaphragm pacer. Inset: the silicon devices. **d**, Photograph of an implanted bipolar cuff electrode to stimulate the PN for DM pacing. **e**, Ultrasound images showing DM twitching and excursion depending on the LED frequencies (vertical red line) ranging from 10 Hz to 50 Hz. **f**, Variations in CMAP amplitudes as a function of V_{pp} during KHFAC stimulation (1 kHz). **g**, Real-time recordings of diaphragmatic EMG, contralateral (left side) and ipsilateral (right side) abdominal movements along the *z* axis (that is, Accel. *Z*) captured using two IMU sensors during KHFAC stimulation (stim.) (1 kHz, V_{pp} = 1.4 V). **h**, Ultrasound images during KHFAC stimulation (top: 5 kHz, V_{pp} = 3.5 V; bottom: 10 kHz, 4 V_{pp}). **i**, Diaphragm excursion (mm) calculated from ultrasound imaging during KHFAC (10 kHz, V_{pp} = 5 V; red) and at pre- (black) and post-KHFAC (blue). Data are shown as points (sample size (*n*): pre = 4, KHFAC = 5, post = 3; one-way ANOVA), based on quantitative data obtained from the ultrasound image shown in Supplementary Fig. 45b). Exact *P* values for the indicated comparisons are pre versus KHFAC, $P < 0.0001$; pre versus post, $P = 0.076$. Box plots show the mean (square marker), median, 1.5 times the interquartile range (1.5× IQR; whiskers) and lower/upper quartiles (boxes).

By contrast, the contralateral left IMU #1 shows only moderately suppressed abdominal movements influenced by the right-side PN stimulation (Fig. 5g, centre). Supplementary Fig. 44b exhibits a frequency dependent blocking effect at a fixed V_{pp} of 1 V, with a reduction as the frequency increases until disappearance of blocking above 5 kHz. This result implies that a higher stimulation frequency requires a higher V_{pp} for blocking. Ultrasound images shown in Fig. 5h indicate that the threshold values of V_{pp} increase with increasing stimulation frequency (for example, 5 kHz, V_{pp} = 3.5 V, Supplementary Video 1; and 10 kHz, V_{pp} = 4 V, Supplementary Video 2), consistent with previous KHFAC studies. Moreover, a reduced temporary muscle twitch (that is, onset response at the initiation of KHFAC) at 10 kHz stimulation compared with 5 kHz (Supplementary Fig. 45a) suggests that higher-frequency stimulation can provide a more effective conduction block of PN. The abovementioned onset response completely disappears for stimulation at 10 kHz and V_{pp} = 5 V (Supplementary Fig. 45b and Supplementary Video 3), indicating complete, rapid and reversible electronic nerve conduction block. Figure 5i shows the mean of diaphragm excursion calculated from ultrasound imaging. The mean ± standard error of the mean values for pre, KHFAC (10 kHz, V_{pp} = 5 V) and post conditions are 2.75 ± 0.13 mm (n = 4), 0.75 ± 0.05 mm (n = 5) and 3.1 ± 0.12 mm (n = 3), respectively.

Conclusions

We have shown that ultrathin b-PTs can serve as remote, optical control elements in electrical circuits designed for wirelessly powered bioresorbable electrical stimulators. By using programmed exposure to NIR light that penetrates through deep tissue, our system can generate diverse stimulation waveforms including monophasic, biphasic and polyphasic output patterns. With the system, which is powered by inductive coupling to a single receiving coil in a compact platform, we demonstrated cardiac pacing in large animal models with biphasic stimulation at single sites or multiple locations, aligning with protocols used to treat cardiac patients. We also demonstrated light-controlled modulation of PNMS in a rodent model using monophasic and polyphasic KHFAC waveforms, for diaphragm pacing and reversible PN blocking to treat respiratory dysfunction, respectively.

Further miniaturized versions of these devices could potentially be fabricated by combining the b-PT control strategy with wireless power transfer methods that eliminate the need for the receiving coil. Furthermore, the crosstalk that results from separate illumination on different phototransistors in a single device could be overcome with wavelength-selective activation, achieved by mounting narrowband filters above the phototransistors[7]. Response times and the photocurrent of the phototransistors could also be improved using NPN rather than PNP doping profiles. In addition, wearable devices with multimodal sensing and in-sensor processing functions could be developed to enable closed-loop control algorithms.

Methods

Fabrication of bioresorbable silicon electronics

b-PTs. Supplementary Fig. 3 shows cross-sectional illustrations of the process for fabricating PNP b-PTs. The process began with standard cleaning procedures defined by Radio Corporation of America (RCA) to remove organic and inorganic contaminants from the surface of the SOI wafer (boron-doped p-type, 5 µm top silicon, 1–10 Ω cm resistivity, 1 µm BOX, Ultrasil LLC), which serves as the collector region (~10^{15} boron ions cm^{-3}). Photolithography defined the phosphorus (n-type) doping area, followed by ion implantation to form the base region with a doping concentration of less than 10^{17} phosphorus ions cm^{-3}. After removing the photoresist (PR) layer and performing RCA cleaning, dry oxidation at 1,000 °C for 7 h activated the ion-implanted dopants and formed a 180-nm thermally grown SiO_2 layer as a doping mask for the emitter region (100 × 100 μm^2). Subsequent photolithography and 6:1 buffered oxide etchant (BOE) wet etching of the SiO_2 layer exposed the areas for the following doping process. After removing PR and performing an additional RCA cleaning, patterned solid-state doping of boron (p-type) at 1,000 °C for 20 min formed p^+ regions for the emitter and collector electrodes, with a doping concentration of higher than 10^{19} boron ions cm^{-3}. After complete etching of the underlying BOX layer by immersion in HF (see details in the following section), patterned deposition of 200-nm-thick SiO_2 and 200-nm-thick W by sputtering deposition and electron beam evaporation, respectively, created a passivation layer and contact metal for the emitter and collector regions.

PIN diode. Plasma-enhanced chemical vapour deposition (PECVD) formed a 300-nm-thick SiO_2 layer as a mask for the doping process on the aforementioned SOI wafer (boron-doped p-type, 5 µm top silicon). Subsequent photolithography and 6:1 BOE wet etching of the SiO_2 layer exposed the surface of the Si for impurity doping. After removing the PR and cleaning the surface, patterned solid-state doping of phosphorus at 950 °C for 20 min defined the n^+ region for the cathode. A second 300-nm-thick SiO_2 layer was then deposited via PECVD as a mask for the next doping process. Photolithography, SiO_2 etching and surface cleaning created the p^+ region for the anode. After complete etching of the underlying BOX layer, the insulator and contact metal were deposited using the same procedure as described above.

MOS capacitors. Using the aforementioned SOI wafer (boron-doped p-type, 5 µm top silicon), a 300-nm-thick SiO_2 is deposited via PECVD. Photolithography and wet etching of the SiO_2 layer expose the silicon surface for impurity doping. After removing the PR and cleaning the surface, patterned solid-state doping of phosphorus at 950 °C for 20 min defined the n^+ region, serving as a heavily doped bottom layer. After complete etching of the underlying BOX layer, patterned deposition formed a 50-nm-thick SiO_2 layer and a 100-nm-thick W layer, as the dielectric and top metal layer, respectively. Variations in the overlapping area between the bottom n^+ layer and the top metal layer influenced the capacitance value, which ranged from 0 pF to 200 pF (Supplementary Fig. 18).

Release and transfer printing

To release the Si electronic components, including b-PTs, PIN diodes and MOS capacitors fabricated on the SOI wafers, photolithography and reactive ion etching (Samco RIE-10NR) are used to create via holes in triangular array geometries (centre-to-centre spacing 150 µm),

exposing the surface of the BOX layer (Supplementary Fig. 3(iv)). Immersing the device in an HF solution completely removed the BOX layer (Supplementary Fig. 3(v)), allowing the components to gently settle onto the surface of the handle wafer. After sequential patterned deposition of the insulator and contact metal to complete the device fabrication, a polydimethylsiloxane (PDMS; Sylgard 184, Dow Corning; base-to-curing-agent ratio of 10:1) stamp was used to retrieve the components for transfer to a bioresorbable substrate by transfer printing (Fig. 2a).

Characterization of the b-PTs

The doping concentration of the b-PT was measured by a commercial analytical service laboratory (QSpec Technology) using SIMS to analyse the depth composition of the vertical junction. Silvaco TCAD software was used to simulate the doping concentration profile, wavelength dependency and transient performance (see Supplementary Note 1 for a detailed description). *I*–*V* characteristics and output photocurrent at an applied V_{EC} were measured using a semiconductor parameter analyser (4155C, Agilent). The light intensity output was examined by an optical power and energy meter (PM200, THORLABS GmbH). Commercial LEDs (MTMD6788594SMT6, Marktech Optoelectronics; SBM-40-RGBW-SC41-QD100, Luminus Devices; and VSMY3850X01-GS08, Vishay Semiconductor Opto Division) were used as light sources to characterize the wavelength dependence and output photocurrent of printed b-PTs on the bioresorbable substrate. The relative responses (%) from the experiment and simulation were normalized to the maximum current output at wavelengths of 623 nm and 600 nm. To calculate the response time (t_r and t_f) of the b-PT, a pulse of light from an 850-nm-wavelength LED was generated using a single-channel function generator (33250A, Agilent), while an oscilloscope (TBS1032B, Tektronix) measured the output voltage (V_L) according to load resistance (R_L), as described in Supplementary Fig. 10a.

Laser-cutting for receiving coils and interconnects of Mo

Spin-casting PDMS on a glass substrate at 2,000 rpm for 30 s, followed by degassing the sample under vacuum to remove the air bubbles, then baking on a hot plate at 110 °C for 5 min, produced a supporting substrate to temporarily mount a foil of Mo (15 and 25 μm thick) during the laser ablation process. Picosecond laser pulses (ProtoLaser R4, LPKF) defined the border outline of the receiving coils and interconnects. The Mo coils were transferred onto a photopolymerized PA film using a PDMS mould (see details in the following section). The Mo interconnects were carefully released from the PDMS-coated glass substrate for subsequent assembly of the electrical stimulator.

Assembly of the electrical stimulator

Figure 3a shows schematic illustrations of the process for assembly of a monolithically integrated, bioresorbable, wireless electrical stimulator. The process began with the preparation of a PDMS mould using standard processes. Specifically, spin-casting a layer of a photodefinable epoxy (SU 8 100) on a Si wafer substrate, followed by photolithography, created features in the required geometry. A layer of polymethylmethacrylate (3,000 rpm for 30 s, curing at 180 °C for 1 min on a hot plate) spin-cast on these structures facilitated release of the PDMS cast and cured on top of them. Pouring PDMS precursor (Sylgard 184, Dow Corning; base-to-curing-agent ratio of 10:1) on the polymethylmethacrylate-coated structure, followed by degassing the sample under vacuum to remove the air bubbles, then baking into a convection oven at 75 °C overnight, produced a solid PDMS replica of the SU 8 features. To release the Mo coils from the PDMS-coated glass substrate (Supplementary Fig. 13(i)), a PDMS mould designed to align with the Mo coils was gently pressed onto the substrate, creating a temporary bond between the mould and the underlying substrate (Supplementary Fig. 13(ii)). Capillary filling delivered a UV-curable PA in its un-crosslinked liquid state into the channels formed by contact of the mould with the substrate (Supplementary Fig. 13(iii)). UV exposure solidified the PA by photopolymerization, to allow release of the Mo coils upon removal of the PDMS mould. The surfaces of the PA in contact with the PDMS were partially cured (semi-solidified) due to the oxygen inhibition effect of the free-radical polymerization process. These process steps were repeated using another PDMS mould with a hinge structure to form the surface of the partially cured PA, enriched with acrylic functional groups (C=C) (Supplementary Fig. 13(iv, v, vi)). After folding the top and bottom layers at the hinge, additional UV exposure allows chemical bonding at the interface of two layers, resulting in a double-layered receiving coil fully encapsulated by PA (Supplementary Fig. 13(vii)).

Electromagnetic simulation of the Mo receiving coil

The commercial software Ansys HFSS (Version 2021 R2) was used to study the electromagnetic behaviour of the single receiver coil. An adaptive mesh (tetrahedron elements), together with a spherical surface as the radiation boundary, was adopted to ensure computational accuracy. The impedance *Z* of the receiver coil was output, and the quality factor *Q* is defined as $Q = |\mathrm{Im}(Z)/\mathrm{Re}(Z)|$, where Re(*Z*) and Im(*Z*) are the real and imaginary parts of the impedance *Z*. The conductivity, relative permittivity and relative permeability used in the simulation were $\sigma_{Mo} = 1.76 \times 10^7$ S m^{-1}, $\varepsilon_{Mo} = 1$ and $\mu_{Mo} = 1$ for molybdenum; and $\sigma_{PA} = 0$ S m^{-1}, $\varepsilon_{PA} = 4.4$ and $\mu_{PA} = 1$ for the PA encapsulant, fitted to match the experimental resonance frequency.

Benchtop studies for light-controlled waveform generation and multisite stimulation

A function generator (33250A, Agilent) supplied power with a frequency of 13.56 MHz and a peak-to-peak voltage (V_{pp}) of 5 V to the transmitting coil (width and length of 15 mm and 24 mm, respectively) for wireless inductive power transfer to the receiving coil (a double-layered Mo coil with an outermost diameter of 16 mm) at a 1-mm coupling distance. An oscilloscope (TBS1032B, Tektronix) measured the output voltage (V_L) according to capacitance values. During wireless power transfer via inductive coupling, various voltages were applied to an 850-nm-wavelength LED mounted on an fPCB using another function generator (DG1022Z, Rigol) to generate different monophasic waveforms such as rectangular, triangular and sinusoidal pulses by adjusting the intensity of light to illuminate the b-PTs. To validate multisite stimulation and the generation of biphasic and polyphasic KHFAC waveforms, two LEDs mounted on an fPCB (centre-to-centre spacing 2 cm) were connected to separate channels of a function generator (DG1022Z, Rigol). The applied voltage and duration were then adjusted for demonstration purposes. An oscilloscope (TBS1032B, Tektronix) was used to measure the output voltage (V_L) across an R_L of 1 kΩ, 1 kΩ and 0.3 kΩ for monophasic, biphasic and polyphasic KHFAC waveforms, respectively.

Development of a wearable device with dual LEDs and its control system

A wearable device with dual LEDs (Supplementary Fig. 23a) capable of latency-adjustable light stimulation integrated a Bluetooth system-on-chip (SoC), LEDs and wireless charging components on a fPCB. The 32-kHz internal clock of the Bluetooth SoC precisely controlled the emission timing of the dual LEDs (AC3535B-YRR-1000mA-H1, Solidlite). On the fPCB, a serpentine structure interconnected the two LEDs, for simultaneous light emission or with adjustable latencies in increments of approximately 30 μs, controlled via general-purpose input/output and the 32-kHz clock. To enable wireless charging, a charging coil with a resonant frequency of 13.56 MHz was designed on the fPCB. RF power transmitted through the coil was rectified, regulated and used to charge a 3.7 V lithium polymer battery (110 mAh) via an integrated battery charging circuit. Customized firmware was uploaded to the Bluetooth SoC using Segger Embedded Studio.

The app also allows users to select operation modes, including single-LED and dual-LED control for monophasic and biphasic stimulation through a graphical user interface (such as smartphone (iPhone XS)). The output intensity of the wearable 850-nm LED module is approximately 265 mW cm^{-2}.

Development of a wearable device with dual IMUs and its data collection system

A wearable device with dual IMUs (Supplementary Fig. 23b), capable of physiological signal monitoring (for example, abdominal movements, cardiac activity and respiratory signals), integrated a Bluetooth SoC, IMUs and wireless charging components on an fPCB. The module used a Bluetooth SoC (ISP-1807, Insight SIP) to transmit IMU data to a mobile device at 20-ms intervals. On the fPCB, a serpentine interconnect structure mechanically decoupled the two IMUs (LSM6DSL, STMicroelectronics), enabling independent operation. These IMUs collected three-axis acceleration data (x, y and z axes) at a sampling rate of 10^4 Hz via serial peripheral interface communication protocols. The wireless charging components and circuit were identical to those of the LED module. Customized firmware was uploaded to the Bluetooth SoC using Segger Embedded Studio. IMU data transmitted via Bluetooth were visualized in real time on the smartphone display (iPhone XS) as three-axis acceleration plots on a customized iOS app developed with Xcode.

In vivo cardiac pacing demonstration in small-animal models

Adult Sprague-Dawley rats (12 weeks old; sourced from Charles River Laboratories), male ($n = 2$), weighing between 200 g and 250 g, were used in this procedure. Isoflurane gas in oxygen induced anaesthesia. Toe reflex was checked to ensure complete anaesthesia. ECG, respiration rate and/or body temperature were monitored. A scalpel incision was made below the axilla at the left fifth intercostal space. A 5-0 silk retraction suture and a microretractor were used to pull up the soft tissues. The device was attached to the heart using sutures or bioadhesives. The device was placed on the exposed anterior epicardial surface of the LV of the heart. Animals were kept under the anaesthesia plane while we tested the device (by performing sensing/pacing protocols). After device testing was completed, the heart was removed from the chest cavity, resulting in euthanasia of the animal by exsanguination. All procedures were carried out in accordance with the National Institutes of Health (NIH) Guide for the Care and Use of Laboratory Animals and were approved by the Institutional Animal Care and Use Committee (protocol IS00021087) of Northwestern University.

In vivo cardiac pacing demonstration in large-animal models

Hound dogs (age 0.7–1.1 years, weight 22–40 kg, sourced from a US Department of Agriculture Class A breeder) were used in this procedure. The animal was positioned in right lateral recumbency on a recirculating water blanket, and the femoral triangle(s) and left lateral thorax were clipped and cleaned. Warm blankets and/or a Bair-Hugger was placed over the head and neck and hindquarters to assist in normothermia. A femoral artery was percutaneously catheterized for monitoring of invasive arterial blood pressure. If percutaneous access was unsuccessful, a vascular cutdown was performed as described below. ECG electrodes were placed on the chest (3M Red Dot) and connected to a PowerLab 4/26 with a Dual Bio Amplifier (acquired and recorded by using LabChart software (AD Instruments)). After preemptive local analgesia was administered and appropriate anaesthetic depth was verified via haemodynamic status, jaw tone and palpebral reflex, a short-acting neuromuscular blocking agent (cisatracurium) was administered to facilitate the surgical thoracotomy approach. A left lateral thoracotomy was performed at the 4th to 6th intercostal space, and the pericardium was incised to visualize the cardiac structures. Following haemodynamic stabilization, epicardial pacing electrodes were placed on the target pacing location. Dogs were euthanized under anaesthesia via exsanguination. A bolus dose of heparin was administered before cardiac excision to prevent vascular thrombosis. The heart was excised for tissue collection. All procedures were carried out in accordance with the NIH Guide for the Care and Use of Laboratory Animals and were approved by the Institutional Animal Care and Use Committee (protocols IS00020402 and IS00027808) of Northwestern University, University of Chicago (protocol 72761).

In vivo PN surgery in small-animal models

The procedure follows a previously reported protocol[51]. Adult Sprague-Dawley rats (12 weeks old; sourced from Charles River Laboratories), male or female, weighing between 200 g and 250 g, were used in this procedure. Before surgery, all surgical tools were thoroughly sterilized. Isoflurane gas in oxygen, with subcutaneous administration of meloxicam, induced anaesthesia. Bupivacaine was then administered subcutaneously at the midline of the neck, targeting the most superficial layer. A 2-cm midline incision through the skin and superficial cervical fascia exposed the sternohyoid and sternocleidomastoid muscles. The sternocleidomastoid was gently elevated using a blunt dissection probe, then retracted laterally using a vessel loop. After gently retracting the omohyoid, the PN was exposed by dissecting between the scalene muscles. The cuff electrode was wrapped around the PN and firmly secured with sutures (Supplementary Fig. 35). The receiving coil of the diaphragm pacer was implanted in the chest subcutaneously. The skin was then closed with interrupted inverted absorbable sutures in the deep dermis. Meloxicam was administrated again for 24 h after surgery. All procedures were carried out in accordance with the NIH Guide for the Care and Use of Laboratory Animals and were approved by the Institutional Animal Care and Use Committee (IACUC) of Northwestern University (protocol IS00017562).

Measurement of EMG

Direct needle recordings from the hemidiaphragm were obtained using a 30-gauge concentric needle EMG electrode (TE/D64-551; Technomed USA) connected with a clinical grade Nicolet EDX system with Synergy software (Natus Neurology). One needle electrode was inserted transcutaneously into the right hemidiaphragm and used to record spontaneous respiratory signals. CMAPs were recorded at the hemidiaphragm, allowing adjustment of electrical stimulation voltage to deliver supramaximal activation of the PN. All recordings were made with concentric needle electrodes (TE/D64-551, Technomed USA).

Measurement of ultrasonography

A GE LOGIQ high-performance ultrasound system was used to detect diaphragmatic excursions. Rats were placed supine. Ultrasound probes were placed on the rats' abdomen to visualize the diaphragm transhepatically. The M mode was used to measure the diaphragm excursion. Based on the mean ± standard error of the mean, a one-way analysis of variance (ANOVA) was performed for statistical tests (Fig. 5i; based on the quantitative data obtained from the ultrasound images shown in Supplementary Fig. 45b).

Reporting summary

Further information on research design is available in the Nature Portfolio Reporting Summary linked to this article.

Data availability

Source data are provided with this paper. Other data that support the findings of this study are available from the corresponding authors upon reasonable request.

Code availability

Customized iOS apps (user interfaces) developed with Xcode for use on smartphones are available from the corresponding author upon reasonable request.

References

1. Zhang, Y. et al. Advances in bioresorbable materials and electronics. *Chem. Rev.* **123**, 11722–11773 (2023).
2. Maurus, P. B. & Kaeding, C. C. Bioabsorbable implant material review. *Oper. Tech. Sports Med.* **12**, 158–160 (2004).
3. Prakasam, M. et al. Biodegradable materials and metallic implants—a review. *J. Funct. Biomater.* **8**, 44 (2017).
4. Singh, R., Bathaei, M. J., Istif, E. & Beker, L. A review of bioresorbable implantable medical devices: materials, fabrication, and implementation. *Adv. Healthc. Mater.* **9**, 2000790 (2020).
5. Han, W. B., Lee, J. H., Shin, J.-W. & Hwang, S.-W. Advanced materials and systems for biodegradable, transient electronics. *Adv. Mater.* **32**, 2002211 (2020).
6. Kang, S.-K. et al. Bioresorbable silicon electronic sensors for the brain. *Nature* **530**, 71–76 (2016).
7. Bai, W. et al. Bioresorbable photonic devices for the spectroscopic characterization of physiological status and neural activity. *Nat. Biomed. Eng.* **3**, 644–654 (2019).
8. Son, D. et al. Bioresorbable electronic stent integrated with therapeutic nanoparticles for endovascular diseases. *ACS Nano* **9**, 5937–5946 (2015).
9. Zhang, Y. et al. Self-powered, light-controlled, bioresorbable platforms for programmed drug delivery. *Proc. Natl Acad. Sci. USA* **120**, e2217734120 (2023).
10. Lee, D.-M. et al. An on-demand bioresorbable neurostimulator. *Nat. Commun.* **14**, 7315 (2023).
11. Koo, J. et al. Wireless bioresorbable electronic system enables sustained nonpharmacological neuroregenerative therapy. *Nat. Med.* **24**, 1830–1836 (2018).
12. Choi, Y. S. et al. Fully implantable and bioresorbable cardiac pacemakers without leads or batteries. *Nat. Biotechnol.* **39**, 1228–1238 (2021).
13. Li, P. et al. Monolithic silicon for high spatiotemporal translational photostimulation. *Nature* **626**, 990–998 (2024).
14. Zhang, Y. et al. Millimetre-scale bioresorbable optoelectronic systems for electrotherapy. *Nature* **640**, 77–86 (2025).
15. Choi, Y. S. et al. A transient, closed-loop network of wireless, body-integrated devices for autonomous electrotherapy. *Science* **376**, 1006–1012 (2022).
16. Kim, E. et al. Electrical stimulation for therapeutic approach. *Interdiscip. Med.* **1**, e20230003 (2023).
17. Pettersen, E., Anderson, J. & Ortiz-Catalan, M. Electrical stimulation to promote osseointegration of bone anchoring implants: a topical review. *J. NeuroEng. Rehabil.* **19**, 31 (2022).
18. Kilgore, K. L. & Bhadra, N. Reversible nerve conduction block using kilohertz frequency alternating current. *Neuromodulation* **17**, 242–254 (2014).
19. Wang, Q. et al. Lead-free dual-frequency ultrasound implants for wireless, biphasic deep brain stimulation. *Nat. Commun.* **15**, 4017 (2024).
20. Piallat, B. et al. Monophasic but not biphasic pulses induce brain tissue damage during monopolar high-frequency deep brain stimulation. *Neurosurgery* **64**, 156–163 (2009).
21. Kavanagh, K. M. et al. Monophasic versus biphasic cardiac stimulation: mechanism of decreased energy requirements. *Pacing Clin. Electrophysiol.* **13**, 1268–1276 (1990).
22. Dopp, A. L., Miller, J. M. & Tisdale, J. E. Effect of drugs on defibrillation capacity. *Drugs* **68**, 607–630 (2008).
23. Scholten, M., Szili-Torok, T., Klootwijk, P. & Jordaens, L. Comparison of monophasic and biphasic shocks for transthoracic cardioversion of atrial fibrillation. *Heart* **89**, 1032–1034 (2003).
24. Ricoy, J. et al. Diaphragmatic dysfunction. *Pulmonology* **25**, 223–235 (2019).
25. Hong, M. K., Han, A. Y. & Long, J. L. Intractable hiccups caused by diaphragmatic eventration. *Cureus* **14**, e24430 (2022).
26. Wang, B. et al. Diaphragmatic dysfunction associates with dyspnoea, fatigue, and hiccup in haemodialysis patients: a cross-sectional study. *Sci. Rep.* **9**, 19382 (2019).
27. Yu, K. J. et al. Bioresorbable silicon electronics for transient spatiotemporal mapping of electrical activity from the cerebral cortex. *Nat. Mater.* **15**, 782–791 (2016).
28. Huang, L.-Y., Zhu, S., Cui, R. & Zhang, M. Noninvasive in vivo imaging in the second near-infrared window by inorganic nanoparticle-based fluorescent probes. *Anal. Chem.* **92**, 535–542 (2020).
29. Feng, Z. et al. Perfecting and extending the near-infrared imaging window. *Light Sci. Appl.* **10**, 197 (2021).
30. Lyu, Y., Li, J. & Pu, K. Second near-infrared absorbing agents for photoacoustic imaging and photothermal therapy. *Small Methods* **3**, 1900554 (2019).
31. Bashkatov, A. N., Genina, E. A. & Tuchin, V. V. Optical properties of skin, subcutaneous, and muscle tissues: a review. *J. Innov. Opt. Health Sci.* **4**, 9–38 (2011).
32. Zhou, N. et al. Effect of pulse phase duration on forward masking and spread of excitation in cochlear implant listeners. *PLoS ONE* **15**, e0236179 (2020).
33. Lee, Y. K. et al. Dissolution of monocrystalline silicon nanomembranes and their use as encapsulation layers and electrical interfaces in water-soluble electronics. *ACS Nano* **11**, 12562–12572 (2017).
34. Choi, Y. S. et al. Biodegradable polyanhydrides as encapsulation layers for transient electronics. *Adv. Funct. Mater.* **30**, 2000941 (2020).
35. Lee, G. et al. A bioresorbable peripheral nerve stimulator for electronic pain block. *Sci. Adv.* **8**, eabp9169 (2022).
36. Kottink, A. I. et al. A randomized controlled trial of an implantable 2-channel peroneal nerve stimulator on walking speed and activity in poststroke hemiplegia. *Arch. Phys. Med. Rehabil.* **88**, 971–978 (2007).
37. Chae, J., Sheffler, L. & Knutson, J. Neuromuscular electrical stimulation for motor restoration in hemiplegia. *Top. Stroke Rehabil.* **15**, 412–426 (2008).
38. Sarr, M. G. et al. The EMPOWER study: randomized, prospective, double-blind, multicenter trial of vagal blockade to induce weight loss in morbid obesity. *Obes. Surg.* **22**, 1771–1782 (2012).
39. Elliott, M. K. et al. Multi-lead pacing for cardiac resynchronization therapy in heart failure: a meta-analysis of randomized controlled trials. *Eur. Heart J. Open* **2**, oeac013 (2022).
40. Trout, M. A., Harrison, A. T., Brinton, M. R. & George, J. A. A portable, programmable, multichannel stimulator with high compliance voltage for noninvasive neural stimulation of motor and sensory nerves in humans. *Sci. Rep.* **13**, 3469 (2023).
41. Thakor, N. V., Ranjan, R., Rajasekhar, S. & Mower, M. M. Effect of varying pacing waveform shapes on propagation and hemodynamics in the rabbit heart. *Am. J. Cardiol.* **79**, 36–43 (1997).
42. Barsheshet, A. et al. Atrial burst pacing with biphasic and monophasic waveforms for atrial fibrillation. *Ann. Noninvasive Electrocardiol.* **17**, 22–27 (2012).
43. Thanaboriboon, C., Vargas, M. A., Alexopoulos, K. & Perez, J. Phrenic nerve block for diaphragmatic pain: case report. *A A Practice* **18**, e01816 (2024).
44. Dontukurthy, S., Biswas, S., Kinthala, S., Housny, W. & Tobias, J. D. Phrenic nerve blockade to diagnose and treat diaphragmatic pain after surgical repair of congenital diaphragmatic eventration. *J. Med. Cases* **11**, 94–96 (2020).
45. Gu, X. Y. et al. Restoration methods of respiratory function for spinal cord injury. *Math. Probl. Eng.* **2020**, 7398789 (2020).
46. Peckham, P. H. & Knutson, J. S. Functional electrical stimulation for neuromuscular applications. *Annu. Rev. Biomed. Eng.* **7**, 327–360 (2005).

47. Testelmans, D. et al. Feasibility of diaphragm pacing in patients after bilateral lung transplantation. *Clin. Transplant.* **31**, e13134 (2017).
48. Chung, J. M. et al. Temporary diaphragm pacing for patients at risk of prolonged mechanical ventilation after extensive aortic repair. *J. Vasc. Surg. Cases Innov. Tech.* **9**, 101319 (2023).
49. Jeong, H. et al. Differential cardiopulmonary monitoring system for artifact-canceled physiological tracking of athletes, workers, and COVID-19 patients. *Sci. Adv.* **7**, eabg3092 (2021).
50. Yoo, J.-Y. et al. Wireless broadband acousto-mechanical sensing system for continuous physiological monitoring. *Nat. Med.* **29**, 3137–3148 (2023).
51. Wang, H. et al. Implantation and control of wireless, battery-free systems for peripheral nerve interfacing. *J. Vis. Exp.* **176**, e63085 (2021).

Acknowledgements

This work was supported by the Querrey-Simpson Institute for Bioelectronics at Northwestern University. This work was supported by the National Research Foundation of Korea (NRF) grant funded by the Korea government (MSIT) (RS-2023-00253677, J.U.K.). This work made use of the NUFAB facility of Northwestern University's NUANCE Center, which has received support from the SHyNE Resource (NSF ECCS-2025633), the IIN, and Northwestern's MRSEC programme (NSF DMR-2308691). J.Z. and Z.M. were supported by a DoD grant: W81XWH2010655. J.-Y.Y. acknowledges funding from the Basic Research Laboratory (BRL) Project from the National Research Foundation (RS-2024-00406674) funded by the Ministry of Science and ICT of Korea. I.R.E. and E.R. were supported by the NIH grants HL141470 and HL165002 and the Leducq Foundation for Cardiovascular Research under award number AWD00001180. A.P. was supported by NIH grant K08HL169904. A.M. and R.K.A. were supported by the NIH grants 1R35HL161249-01 and RO1 HL168117-01. C.K.F. acknowledges support from the National Institute of Neurological Disorders and Stroke (R01NS136683), the American Neuromuscular Foundation (Neuromuscular Grant), and the Belle Carnell Regenerative Neurorehabilitation Fund at the Shirley Ryan AbilityLab. This research was supported by the National Research Foundation of Korea (NRF), funded by the Ministry of Science, ICT and Future Planning (NRF-2024-00347660, S.H.J.). CT imaging work was supported by the Center for Translational Imaging at Northwestern University (RRID:SCR_017878), generously supported by NIH HEI award 1S10OD032221-01A1.

Author contributions

J.U.K., S.G.S. and J.A.R. conceived the concepts and planned the studies. J.U.K., S.G.S., J.Z., J.C., J.K, S.Y.P., J.J., S.K., Y.Z., R.F.N., D.-H.S., S.C., Y.J.J., Z.M. and S.H.J. fabricated and characterized b-PTs. J.G., J.Z. and Z.M. performed computational simulations. J.U.K., S.G.S., H.W., E.R., A.P., R.K.A., A.M. and S.W.J. performed in vivo experiments. H.-Y.A., R.F.N., D.-H.S. and J.-Y.Y. prepared the wearable and control modules. J.U.K., S.G.S., H.W., E.R. and J.-Y.Y. analysed the results. S.L and Y.H. performed electromagnetic simulation. J.U.K., S.G.S., H.W., E.R., A.P., R.K.A., A.M., J.-Y.Y., I.R.E., C.K.F., Z.M., S.H.J. and J.A.R. discussed and interpreted the data. H.-Y.A., G.L., Y.J.J., S.M.W., T.-i.K. and Y.H.J. assisted with preparations of figures. J.U.K., S.G.S., H.W., E.R. and J.A.R. wrote the manuscript. J.G., J.-Y.Y., I.R.E., C.K.F., Z.M., S.H.J. and J.A.R. reviewed and edited the manuscript. J.U.K., S.G.S., H.W. and E.R. contributed equally to this work.

Competing interests

The authors declare no competing interests.

Additional information

Supplementary information The online version contains supplementary material available at https://doi.org/10.1038/s41928-026-01655-8.

Correspondence and requests for materials should be addressed to Jae-Young Yoo, Igor R. Efimov, Colin K. Franz, Zhenqiang Ma, Sung Hun Jin or John A. Rogers.

Peer review information *Nature Electronics* thanks Jun Chen, Guosong Hong and Brian Timko for their contribution to the peer review of this work.

[1]Querrey Simpson Institute for Bioelectronics, Northwestern University, Evanston, IL, USA. [2]School of Chemical Engineering, Sungkyunkwan University, Suwon, Republic of Korea. [3]School of Electronic Engineering, Kumoh National Institute of Technology, Gumi, Republic of Korea. [4]Regenerative Neurorehabilitation Laboratory, Shirley Ryan AbilityLab, Chicago, IL, USA. [5]Department of Biomedical Engineering, Northwestern University, Evanston, IL, USA. [6]Department of Electrical and Computer Engineering, University of Wisconsin-Madison, Madison, WI, USA. [7]Department of Electrical and Computer Engineering, Texas A&M University, College Station, TX, USA. [8]Department of Electrical and Computer Engineering, The University of Texas at Dallas, Richardson, TX, USA. [9]Department of Chemical Engineering, Dankook University, Yongin, Republic of Korea. [10]Department of Foundry Engineering, Dankook University, Yongin, Republic of Korea. [11]Department of Electronic Engineering, Hanyang University, Seoul, Republic of Korea. [12]Feinberg Cardiovascular and Renal Research Institute, Feinberg School of Medicine, Northwestern University, Chicago, IL, USA. [13]Biological Sciences Division, Department of Medicine, University of Chicago, Chicago, IL, USA. [14]Weldon School of Biomedical Engineering, Purdue University, West Lafayette, IN, USA. [15]Elmore Family School of Electrical and Computer Engineering, Purdue University, West Lafayette, IN, USA. [16]School of Electrical Engineering, Korea Advanced Institute of Science and Technology, Daejeon, Republic of Korea. [17]Department of Chemical and Biomolecular Engineering, College of Design and Engineering, National University of Singapore, Singapore, Singapore. [18]Department of Materials Science and Engineering, Northwestern University, Evanston, IL, USA. [19]Department of Physics and Astronomy, Northwestern University, Evanston, IL, USA. [20]Department of Chemical Engineering and Applied Chemistry, Kyungpook National University, Daegu, Republic of Korea. [21]Department of Civil and Environmental Engineering, Northwestern University, Evanston, IL, USA. [22]Department of Materials Science and Engineering, Korea Advanced Institute of Science and Technology, Daejeon, Republic of Korea. [23]Department of Electrical and Computer Engineering, University of Southern California, Los Angeles, CA, USA. [24]Department of Electrical and Computer Engineering, Sungkyunkwan University, Suwon, Republic of Korea. [25]Division of Plastic and Reconstructive Surgery, Department of Surgery, Northwestern University Feinberg School of Medicine, Chicago, IL, USA. [26]Biologics Laboratory, Shirley Ryan AbilityLab, Chicago, IL, USA.

[27]Department of Mechanical Engineering, Northwestern University, Evanston, IL, USA. [28]Department of Semiconductor Convergence Engineering, Sungkyunkwan University, Suwon, Republic of Korea. [29]Department of Medicine, Northwestern University, Chicago, IL, USA. [30]Department of Physical Medicine and Rehabilitation, Feinberg School of Medicine, Northwestern University, Chicago, IL, USA. [31]Ken and Ruth Davee Department of Neurology, Feinberg School of Medicine, Northwestern University, Chicago, IL, USA. [32]Department of Medicine (Pulmonary and Critical Care), Feinberg School of Medicine, Northwestern University, Chicago, IL, USA. [33]Department of Physical Therapy and Human Movement Sciences, Feinberg School of Medicine, Northwestern University, Chicago, IL, USA. [34]Department of Information Display, Kyung Hee University, Seoul, Republic of Korea. [35]Department of Neurological Surgery, Feinberg School of Medicine, Northwestern University, Chicago, IL, USA. [36]These authors contributed equally: Jong Uk Kim, Seung Gi Seo, Hongkai Wang, Eric Rytkin. ✉e-mail: jy.yoo@skku.edu; igor.efimov@northwestern.edu; cfranz@sralab.org; mazq@engr.wisc.edu; jinsh@khu.ac.kr; jrogers@northwestern.edu

nature portfolio

Corresponding author(s): John A. Rogers, Sung Hun Jin, Zhenqiang Ma, Colin K. Franz, Igor R. Efimov, Jae-Young Yoo

Last updated by author(s): Apr 21, 2026

Reporting Summary

Nature Portfolio wishes to improve the reproducibility of the work that we publish. This form provides structure for consistency and transparency in reporting. For further information on Nature Portfolio policies, see our Editorial Policies and the Editorial Policy Checklist.

Statistics

For all statistical analyses, confirm that the following items are present in the figure legend, table legend, main text, or Methods section.

n/a	Confirmed
☐	☒ The exact sample size (*n*) for each experimental group/condition, given as a discrete number and unit of measurement
☐	☒ A statement on whether measurements were taken from distinct samples or whether the same sample was measured repeatedly
☐	☒ The statistical test(s) used AND whether they are one- or two-sided *Only common tests should be described solely by name; describe more complex techniques in the Methods section.*
☒	☐ A description of all covariates tested
☒	☐ A description of any assumptions or corrections, such as tests of normality and adjustment for multiple comparisons
☐	☒ A full description of the statistical parameters including central tendency (e.g. means) or other basic estimates (e.g. regression coefficient) AND variation (e.g. standard deviation) or associated estimates of uncertainty (e.g. confidence intervals)
☒	☐ For null hypothesis testing, the test statistic (e.g. *F*, *t*, *r*) with confidence intervals, effect sizes, degrees of freedom and *P* value noted *Give P values as exact values whenever suitable.*
☒	☐ For Bayesian analysis, information on the choice of priors and Markov chain Monte Carlo settings
☒	☐ For hierarchical and complex designs, identification of the appropriate level for tests and full reporting of outcomes
☒	☐ Estimates of effect sizes (e.g. Cohen's *d*, Pearson's *r*), indicating how they were calculated

Our web collection on statistics for biologists contains articles on many of the points above.

Software and code

Policy information about availability of computer code

Data collection	Oscilloscope (TBS1032B; Tektronix), PowerLab 4/26 with a Dual Bio Amp for ECG, Nicolet EDX® system for EMG recording, Customized iOS app developed with Xcode
Data analysis	OriginPro 2024b, Matlab r2023b (Fig 5g, Fig S42b,c and S44b; Z-axis acceleration data), Excel (Office 365), LabChart Version 8 Pro, One-way Anova (Fig. 5i; based on the quantitative data obtained from the ultrasound image shown in Fig. S45b)

For manuscripts utilizing custom algorithms or software that are central to the research but not yet described in published literature, software must be made available to editors and reviewers. We strongly encourage code deposition in a community repository (e.g. GitHub). See the Nature Portfolio guidelines for submitting code & software for further information.

Data

Policy information about availability of data

All manuscripts must include a data availability statement. This statement should provide the following information, where applicable:

- Accession codes, unique identifiers, or web links for publicly available datasets
- A description of any restrictions on data availability
- For clinical datasets or third party data, please ensure that the statement adheres to our policy

The main source data are provided with this paper. Supplementary and additional data are available from the corresponding author upon reasonable request.

Research involving human participants, their data, or biological material

Policy information about studies with human participants or human data. See also policy information about sex, gender (identity/presentation), and sexual orientation and race, ethnicity and racism.

Reporting on sex and gender	N/A
Reporting on race, ethnicity, or other socially relevant groupings	N/A
Population characteristics	N/A
Recruitment	N/A
Ethics oversight	N/A

Note that full information on the approval of the study protocol must also be provided in the manuscript.

Field-specific reporting

Please select the one below that is the best fit for your research. If you are not sure, read the appropriate sections before making your selection.

☒ Life sciences ☐ Behavioural & social sciences ☐ Ecological, evolutionary & environmental sciences

For a reference copy of the document with all sections, see nature.com/documents/nr-reporting-summary-flat.pdf

Life sciences study design

All studies must disclose on these points even when the disclosure is negative.

Sample size	No sample size calculation was performed. Instead, sample sizes in Figs. 4 and 5 were determined based on proof-of-concept experiments and similar electrical stimulation studies (Y.S. Choi et al., Nat. Biotechnol. (2021); G. Lee et al., Sci. Adv. (2022)). These sample sizes were considered sufficient to assess the feasibility of the system and to confirm consistent experimental trends. In Fig. 5i, a sample size of n = 3 or more, based on quantitative data obtained from the ultrasound images shown in Fig. S45b, was used for statistical analysis.
Data exclusions	No data were excluded.
Replication	All bioresorbable samples/devices were successfully prepared by same fabrication processes described in the manuscript. In vivo reproducibility was evaluated by repeating the stimulation experiments with prepared samples/devices and confirming consistent trends in the measured responses. All replication attempts were successful.
Randomization	For in vivo cardiac pacing studies, rat and canine models were randomly assigned to experimental groups. For in vivo phrenic nerve stimulation studies, rat models were randomly assigned to experimental groups.
Blinding	All data were collected in a non-biased manner. In vivo experiement and analysis were performed by different authors. Blinding wouldn't have influenced the experimental results.

Reporting for specific materials, systems and methods

We require information from authors about some types of materials, experimental systems and methods used in many studies. Here, indicate whether each material, system or method listed is relevant to your study. If you are not sure if a list item applies to your research, read the appropriate section before selecting a response.

Materials & experimental systems

n/a	Involved in the study
☒	☐ Antibodies
☒	☐ Eukaryotic cell lines
☒	☐ Palaeontology and archaeology
☐	☒ Animals and other organisms
☒	☐ Clinical data
☒	☐ Dual use research of concern
☒	☐ Plants

Methods

n/a	Involved in the study
☒	☐ ChIP-seq
☒	☐ Flow cytometry
☒	☐ MRI-based neuroimaging

Animals and other research organisms

Policy information about studies involving animals; ARRIVE guidelines recommended for reporting animal research, and Sex and Gender in Research

Laboratory animals	Sprague-Dawley rat model (12 weeks old; weight 200-250 g, sourced from Charles River Laboratories) for cardiac pacing, male (n=2), protocol IS00021087; Northwestern University for phrenic nerve stimulation, male and female, protocol IS00017562; Northwestern University Canine models (hound dogs) for cardiac pacing (age 0.7-1.1 years old; weight 22-40 kg, sourced from USDA Class A breeder) 29.8kg, male DOB 10/19/2023, protocol IS00020402; Northwestern University 24.2kg, male DOB 10/19/2023, protocol IS00020402; Northwestern University 22kg, DOB 11/12/2024, protocol 72761; University of Chicago 40 kg, male DOB 05/18/2024, protocol IS00027808; Northwestern University 23kg, DOB 12/07/2024, protocol 72761; University of Chicago
Wild animals	No wild animals were used in this study.
Reporting on sex	Sex-based study was not perfomed in this study.
Field-collected samples	No field-collected samples were used in this study.
Ethics oversight	All animals received care according to the guidelines for the care and use of laboratory animals of Northwestern University, University of Chicago. All animal experiment was approved by the Institutional Animal Care and Use Committee.

Note that full information on the approval of the study protocol must also be provided in the manuscript.

Plants

Seed stocks	N/A
Novel plant genotypes	N/A
Authentication	N/A